Fluid-driven fractures in granular media: Insights from numerical investigations

Zhuang Sun, Zihao Li, D. Nicolas Espinoza, and Matthew T. Balhoff

Phys. Rev. E **101**, 042903 — Published 22 April 2020

DOI: 10.1103/PhysRevE.101.042903

Fluid-Driven Fractures in Granular Media: New Insights from Numerical Investigations

Zhuang Sun*, Zihao Li, D. Nicolas Espinoza, Matthew T. Balhoff

Hildebrand Department of Petroleum and Geosystems Engineering, The University of Texas at Austin, Austin, Texas, USA

*corresponding author: zhuangsun@utexas.edu; 200 E. Dean Keeton, Stop C0300, Austin, TX 78712-1585

Abstract

We investigate the mechanisms of opening-mode fracture initiation in granular media. The study is based on simulation of grain-scale fluid-grain interactions through a coupled numerical approach in which the discrete element model (DEM) is used to solve for the mechanics of a solid granular medium and computational fluid dynamics (CFD) is used to model fluid flow and drag forces. We present benchmark problems with analytical solutions and validate this numerical model against experiments of viscous-drag driven cavity in the literature. Additional simulation results show fracture initiation mechanisms in a random granular packing subjected to constant boundary stresses and to fluid injection with a localized source. The dimensionless variable F_s/F_{sk} (ratio of seepage force F_s and skeletal force F_{sk}) incorporates the impacts of physical properties and injection parameters including fluid viscosity, injection velocity, grain size and effective stresses, and has been used as a criterion separating regimes of fluid invasion and drag-driven fracture opening. Our simulation results show that F_s/F_{sk} in combination with τ_1 (ratio of diffusion time from hydromechanical coupling and injection time) serve as a prediction of fracture opening within granular packing. We suggest a simple criterion ($F_s/F_{sk} > 1$ or $\tau_1 > 0.17$) that is valid for various types of granular media and injection conditions to determine if fracture opening will occur. Among other applications, this study is useful to predict the initiation and propagation of fractures in natural sediments.

Keywords: Discrete element method; computational fluid dynamics; resolved CFD-DEM approach; viscous-drag driven cavity; regimes of fracture opening.

1. Introduction

Fluid injection into the subsurface occurs in many engineering applications such as CO_2 geological storage [1,2], grouting for ground improvement [3,4], enhanced oil recovery [5], waste subsurface disposal [6,7], and water-flooding for hydrocarbon recovery and hydraulic fracturing [8–12]. Fractures are a common consequence of subsurface fluid injection. Natural fluid overpressure can also force the fluid to migrate through porous media and create localized fractures in geosystems [13–20]. Improved theories and models of fluid-driven fractures in granular media are of great importance to predict natural geosystems and optimize engineering designs.

Elastic solutions, e.g. linear elastic fracture mechanics (LEFM), have been extensively used to investigate the initiation and propagation of fluid-driven fractures in cohesive rocks [21–25]. Elastic formulations are usually not applicable to the unconsolidated formations with little cementation and high permeability due to their lack of tensile strength and strongly coupled behavior with the fluid pressure [6,26–31]. Discrete approaches, e.g. the discrete element method (DEM), treat the rock as an assembly of blocks or particles and allow for a direct investigation of local physical phenomena such as the initiation and formation of cracks [32,33]. Discrete approaches are more realistic at the micro-scale than usual continuum approaches.

There are various models to simulate fluid flow and interaction between fluid and particles based on discrete approaches. Pore network modeling simplifies the complex pore-space geometry as an interconnected network of pores and channels [34]. Pore network modeling based on the discrete element packing overcomes the issue of high computational cost but does not provide an accurate reproduction of the fluid domain [17,35–39]. There are also approaches coupling Smooth Particle Hydromechanics (SPH) or the Lattice Boltzmann Method (LBM) with DEM to describe the fluid-particle system [40–47]. However, these approaches require long computational times and therefore are rarely used to model fluid-driven fractures. Computational fluid dynamics (CFD) coupled with DEM has been widely applied to various hydro-mechanical engineering problems [48–51]. The CFD-DEM model can use either “resolved” or “unresolved” approaches dependent on the size of the particles and the required resolution of fluid flow [52–54]. In this study, we adopt the resolved approach that can capture well the fluid flow within each individual pore and the impact of the two phases (fluid and grain) on each other.

Experimental studies show that micromechanical processes are fundamental to fluid-driven fractures in granular media [55–57]. At the particle level, the most important forces involved in the fluid-driven particle displacements include the weight of particles $W = \pi d_p^3 \rho_f g/6$, where d_p is the particle size and ρ_f is the fluid mass density, the skeletal force $F_{sk} = \sigma d_p^2$, where σ is the effective stress [N/m^2] acting on the particles, the capillary force $F_c = \pi d_p T_s$ due to an injection of immiscible fluid with interfacial tension T_s [N/m], and the seepage force $F_s = 3\pi\mu_f u d_p$ due to an injection of miscible fluid of viscosity μ_f traversing the pore space with a velocity u. Skeletal force scales with d_p^2 while capillary and seepage forces scale with d_p [58]. Therefore, fine grains are more prone to fluid-driven fracture opening with capillary and seepage forces exceeding skeletal force than coarse grains. The van der Waals force describing the interaction between molecules remains negligible for the range of d_p in this study.

Fig. 1 shows various regimes of fracture opening due to invasion of an immiscible and/or miscible fluid [58]. A medium of coarse grains (large d_p) corresponds to zone (a) with no fracturing due to fluid invasion. Capillary forces caused by the immiscible invasion can promote fracture opening in fine-grained media, as shown by zone (b). Fracture initiation driven by miscible fluids requires enough drag force to support opened fracture walls (zone (c)). In other words, fine-grained media, high fluid flow velocity, high fluid viscosity, and low effective confining stress favor fracture opening [29]. Capillary and seepage forces may also induce fracture opening under a mixed mode (zone (d)). Here, we focus on the invasion of miscible fluids (the x-axis in Fig. 1), which results from the competition between seepage and skeletal forces.

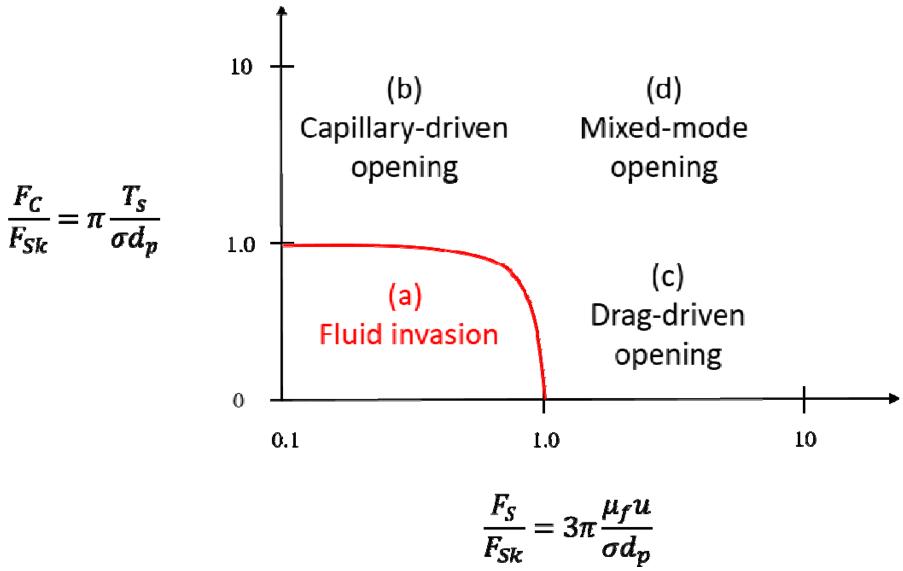

Figure 1. Regimes of fracture opening dependent on fluid and granular medium type and a force balance between capillary (F_c), seepage (F_s) and skeletal forces (F_{sk}) (Re-drawn from [58]). Parameter d_p is the particle size, T_s is the interfacial tension, σ is the effective stress, μ_f is the fluid viscosity and u is the injection velocity.

The objective of this article is to investigate the underlying mechanisms and conditions that determine fracture openings in uncemented granular media. We use a grain-scale fracture initiation model based on the CFD-DEM to model fluid flow through a granular medium. First, we describe the resolved CFD-DEM model which can capture the particle-particle/fluid interactions at high particle concentrations. Second, we validate the numerical model against experiments of fluid-driven deformation of a soft granular material. Last, we discuss the fracture initiation mechanisms in a random granular packing subjected to constant boundary stresses and fluid injection with a localized fluid source. We identify the regimes of fracture opening by combining two dimensionless parameters. This work reveals how particle-scale processes contribute to fluid-driven fracture initiation at the grain scale.

2. Numerical Approach

The solid granular medium is modeled with the discrete element method (DEM) and the fluid flow is solved using computational fluid dynamics (CFD). We implement this coupled model with "CFDEMcoupling", which is an interface between the discrete element code LIGGGHTS and the CFD toolbox OpenFOAM [59]. The CFD-DEM model combines Eulerian and Lagrangian methods [47,52,53,60]. The DEM approximates an individual grain by an idealized shape, e.g. sphere in 3D and disk in 2D, calculates the forces and torques exerted at particle contacts, and explicitly updates the particle dynamics at each iteration through Newton and Euler equations. The contact law follows a Hertzian contact mechanics in between particles. The material properties used for particles include: Young's modulus of particles E, Poisson's ratio v, coefficient of friction μ, mass density ρ_p. The macroscopic mechanical behavior emerges from the interplay of mostly rigid particles through their contacts at the microscale [32]. Detailed model formulation of the DEM can be found in our previous work [61,62]. The CFD is a direct numerical simulation approach to describe the fluid flow and involves the discretization and solution of the Navier-Stokes (N-S) equation in space and time using various numerical methods, e.g. finite volume method in this study [63,64].

In this work, we adopt the resolved CFD-DEM approach to model the solid phase with the fictitious domain method, which is suitable for a complex geometry (particulate phase in this study) embedded in a simple domain [65]. The advantages include that (1) fluid flow is fully resolved without any reduced order models (in contrast to the unresolved approach that solves a locally averaged N-S equation and assumes a drag law of fluid flow on particles); (2) the model has structural rectilinear CFD meshes independent of the particle location and therefore avoids grid regeneration and unstructured meshes that could be computationally expensive; (3) the model has a good scalability which enables parallel implementation. This resolved approach is applicable for large particles covering fine computational mesh cells that simulate the accurate fluid flow and fluid-solid coupling. The supplementary material includes a brief introduction to the model formulation and algorithm. More details can be found elsewhere [52,65].

The supplementary material also presents several classic benchmark problems for the numerical approach: (1) upward seepage flow in a single column of spheres, (2) a settling single spherical particle in a fluid and (3) steady state fluid flow and pressure drop through a random particle packing. The results of the resolved CFD-DEM model agree with the corresponding analytical solutions.

3. Model Validation against Experiments

MacMinn et al. (2015) injected a mixture of water and glycerol (61% glycerol in mass) into the center of radial disk filled with a monolayer of soft spherical polyacrylamide hydrogel particles and studied its deformation during injection [66]. Their system contained ~25,000 spherical particles between two glass plates and was initially fully saturated. The packing had an initial porosity of ~0.51. A permeable spacer separating the two plates confined the outward movement of particles but allowed fluid to flow through. The particles were elastic, non-cohesive, incompressible (Poisson's ratio is ~0.5), slippery (coefficient of friction is near zero) and followed the Hertzian contact model. Table 1 shows the properties of the particles.

Table 1. Properties of soft spherical polyacrylamide hydrogel particles

Young's modulus, E	20 KPa
Poisson's ratio, v	0.4999
Coefficient of friction, μ	0
Mean diameter, d_p	1.2 mm

Fig. 2 shows the experimental setup and the image of the displaced particles at the end of fluid injection. The plate had a circular shape with a radius b of 105 mm. The injection port had a radius of 1.25 mm. The injected fluid had a viscosity of 0.012 Pa·s and was injected at a constant volumetric rate Q (= 16 mL/min). The fluid flowed radially and exited through the annular spacer. The fluid flow dragged the particles outwards and resulted in a cavity at the center. After the deformation reached an equilibrium state, fluid injection stopped and particles relaxed. Therefore, the cavity first opened then closed during the experiment.

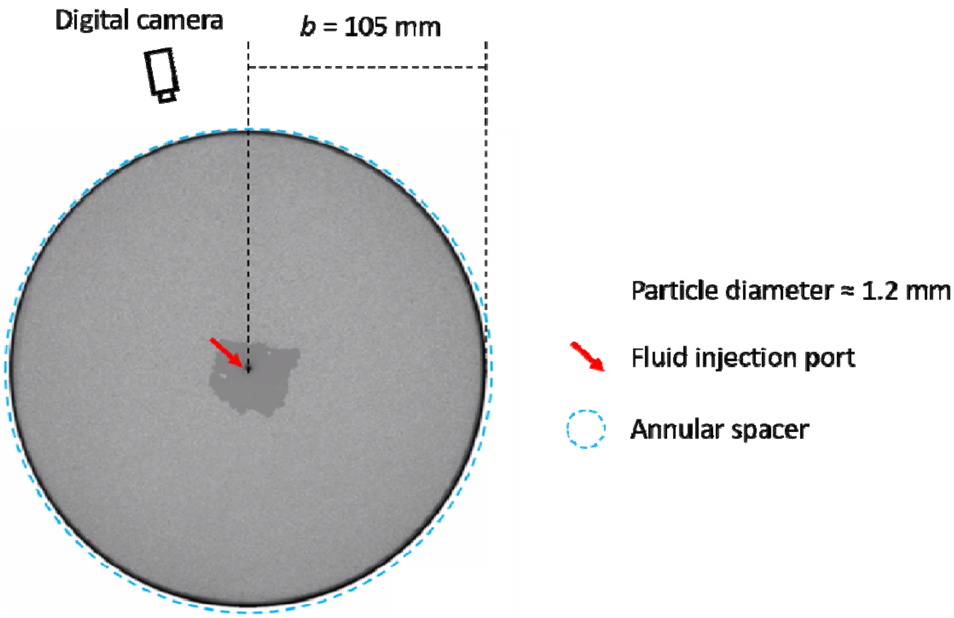

Figure 2. Fluid is injected into a monolayer of soft spherical particles and displaces the particles outwards. The annular spacer confines the particle movement but allows the fluid to flow through. Parameter b is the radius of particle packing. The high-resolution imaging and particle-tracking permit calculating displacements field. The image [66] shows the particle packing at the end of fluid injection.

We simulate the fluid-driven cavity in a packing of soft particles shown in Fig. 2 using the resolved CFD-DEM model. Limited by the computational time, the domain of the simulation ($2b$ = 80 mm) was set smaller than that of the experiment ($2b$ = 210 mm). The particles have a diameter of 1.2 mm. The packing has an initial porosity of ~0.46. Other model parameters are set equal to those in the experiment. Boundary conditions of the fluid flow include a constant injection rate and an atmospheric pressure at the draining spacer. Fig. 3a shows the simulated cavity shapes at steady-state conditions in the experiments. Fig. 3b shows the evolution of the cavity in the numerical simulation. The color represents the absolute particle displacements. Parameter t_D is the dimensionless time and r_D is the dimensionless radius. Similar to the experiment, the fluid injection opens a cavity due to drag forces; then, the injection stops and the cavity closes due to the elastic response of the particles.

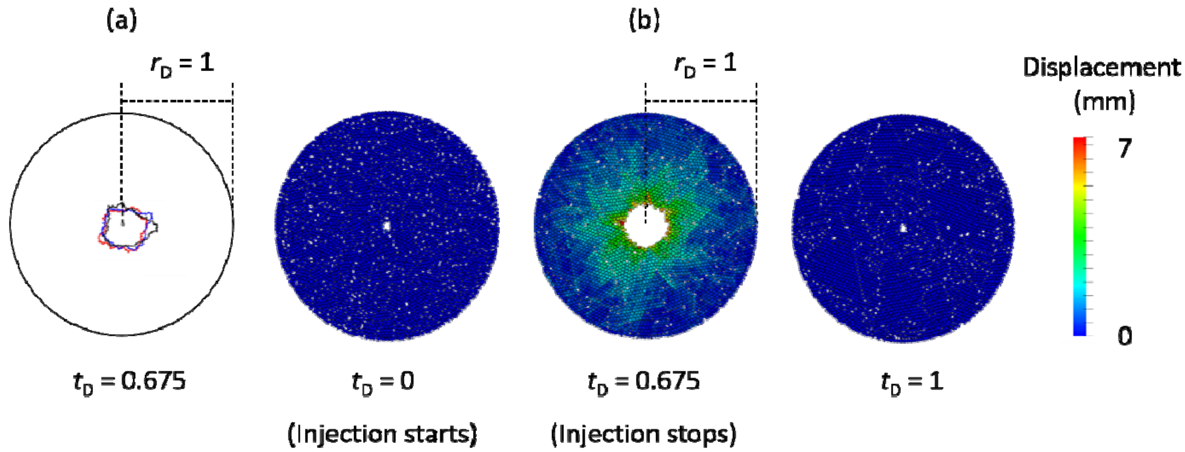

Figure 3. Experimental and numerical results (a) Steady-state cavity shape from three experiments [66]. (b) Absolute displacements of particles in the resolved CFD-DEM simulation. The cavity first opens due to drag forces and then closes when injection stops. Parameter t_D is the dimensionless time and r_D is the dimensionless radius.

The shape of the cavity in the experiments is not repeatable indicating the irreversible micromechanical deformations [66]. The simulated cavity tends to be more symmetric around the injection port and smooth compared to the experimental cavity, which is likely due to the small domain of the numerical simulation and perfect uniform distribution and spherical shape of simulated particles. We normalize the time t and radial position r by the domain radius b and the duration of the experiments/simulation t_{max} (proportional to the characteristic time scale T_{pe}):

$$r_D = \frac{r}{b} \quad (1)$$

$$t_D = \frac{t}{t_{\max}} \quad (2)$$

$$t_{\max} \propto T_{pe} = \frac{\mu_f b^2}{Ek} \quad (3)$$

where μ_f is the fluid viscosity, E is the effective (drained) Young's modulus of the granular medium and k is the permeability of the granular medium [66,67]. The dimensionless cavity area A_D is the ratio of the cavity area A and domain area πb^2:

$$A_D = \frac{A}{\pi b^2} \tag{4}$$

We compare the evolution of dimensionless cavity area A_{D} over the dimensionless time t_{D} from three experiments and our three numerical simulation (Fig. 4). The injection rate Q is constant and equal to 16 mL/min for both experiments and simulations.

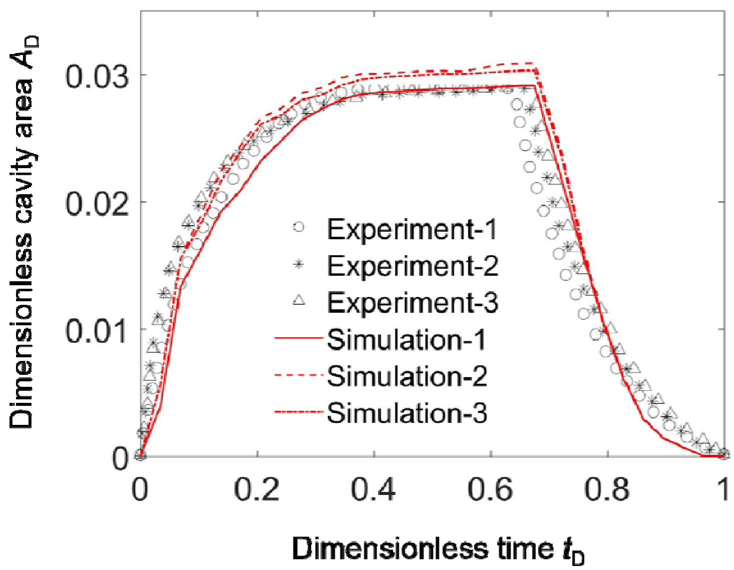

Figure 4. Comparison between three experiments [66] and our three CFD-DEM numerical simulations. The resolved CFD-DEM approach can predict a similar macroscopic deformation behavior because it captures well the fluid-particle and particle-particle interactions.

Fig. 4 shows that the resolved CFD-DEM model can predict the fluid-driven cavities observed in the experiments. The three experiments are a result of the injection-relaxation cycles repeated on the same group of particles. The variability of the results under identical operational conditions indicates that the particle spatial distribution has a slight impact. The change in cavity area results from a force balance between the drag force and the elastic contact force caused by a drag-driven compaction. The resolved CFD-DEM approach can capture well the fluid-particle and particle-particle interactions and therefore predicts a similar macroscopic deformation behavior. The experiments have limitations related to using only one type of soft granular material and having fixed walls radially symmetric. The numerical CFD-DEM model allows changing granular micromechanical properties, fluid characteristics, and boundary conditions. In the following section, we investigate fracture opening induced by fluid injection into a granular medium based on the resolved CFD-DEM approach.

4. Results and Discussion

4.1 Fluid-driven fracture opening with anisotropic state of stress

We investigate the underlying mechanisms of fluid-driven fractures in uncemented granular media under an anisotropic state of stress. The model of granular media is simplified to a numerical packing of 10,122 spherical particles with a diameter of 2 μm in one layer (Fig. 5). The monolayer has no gravity effects. We prepare the grain packing by generating random grains within the simulation domain and relaxing them until negligible grain-to-grain overlaps. The porosity of the sample is conditioned by the initial placement of particles in the simulation domain. The simulation domain is rectangular of 200 μm × 200 μm, which is large enough to eliminate the boundary effects. We apply constant stress boundary conditions in the x- and y-directions and use a stress ratio (maximum stress $\sigma_{\max}$ over minimum stress $\sigma_{\min}$) of $\sigma_{\max}/\sigma_{\min} = 4$, which is close to the critical stress anisotropy that can be imposed without inducing a shear failure [68]. A high stress anisotropy is expected to increase the likelihood of shear failure and facilitate fracture propagation [69]. After the packing is subjected to a given state of stress, the fluid is injected at the inlet port placed at the bottom-center of the model. The porous medium is initially saturated with the same fluid as the fluid we inject. The fluid flows through the particle packing and exits at the boundaries with a prescribed constant outlet pressure. The particles are subjected to constant-stress boundaries and can move after the loading procedure. The CFD mesh is uniform with 4 cells per particle diameter [53]. The Reynold's number (Re) is about 2×10^{-6} at the inlet indicating a laminar flow regime.

$$\mathrm{Re} = \frac{\rho_f u d_p}{\mu_f} \sim 2\times10^{-6} \tag{5}$$

The base case simulation is performed with the parameters given in Table 2 and models the fracturing opening process within a time period of 1 s. The injection hole has a diameter of 2 μm. The fluid injection Darcy velocity is the volumetric injection rate divided by the cross-sectional area of the porous medium, i.e. the perimeter of the injection hole times the thickness of the particle packing. The simulation is run in parallel and takes ~ 48 hours on 192 Xeon E5-2690 v3 (Haswell) 2.6 GHz processors of Lonestar5 high performance computing resource in Texas Advanced Computing Center. All model parameters are typical values of fluid flow and fine granular material [70,71]. We explore the effects of these parameters in the following sections. Please note that a monodisperse packing of spheres can order into crystalline structures and might affect the results. This is a limitation of the current study and has implications on the extension of this work to real subsurface granular media with a particle size distribution. Adding a particle size distribution would add one more level of complexity to the problem that we decided to skip in this study.

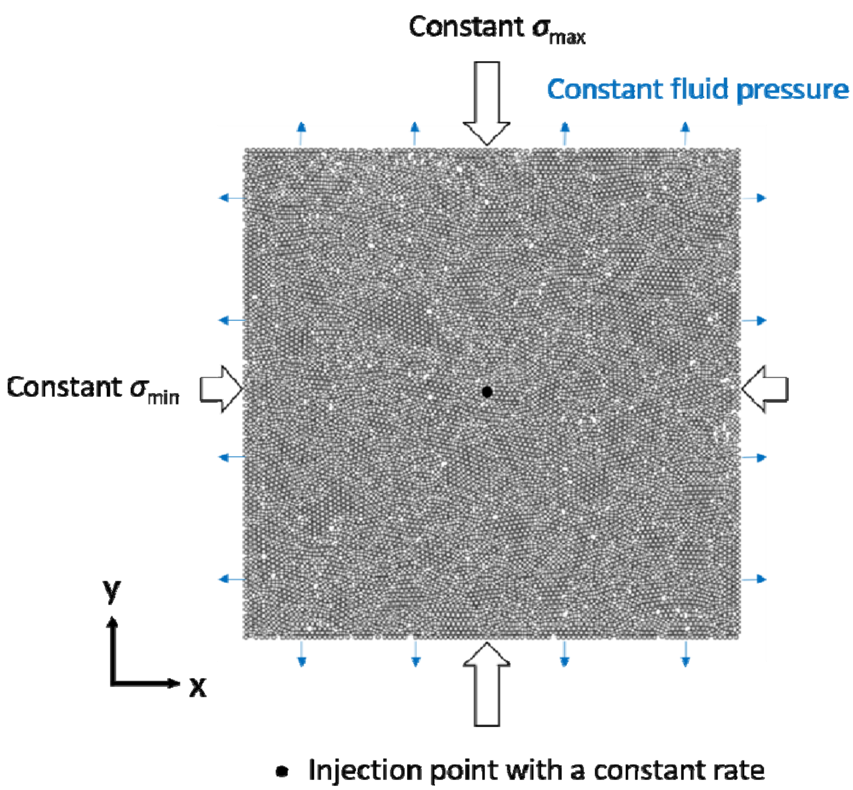

Figure 5. Schematic of CFD and DEM boundary conditions applied to a random particle packing. σ_{max} and σ_{min} are maximum and minimum stresses where σ_{max} = 4×σ_{min}. The fluid is injected from the middle black point with a constant fluid injection rate and exits at the boundaries with a constant fluid pressure.

Table 2. Model parameters of CFD-DEM simulation

Particle Young's modulus, E	1 MPa
Particle Poisson's ratio, v	0.3
Particle-particle/particle-wall coefficient of friction, μ	0.5
Particle diameter, d_p	2 μm
Particle density, ρ_p	2,650 kg/m^3
Maximum stress, σ_{max}	2.5 KPa
Fluid injection Darcy velocity, u	1 mm/s
Fluid viscosity, μ_f	1 Pa·s
Fluid density, ρ_f	1,000 kg/m^3
Number of particles	10,122

Fig. 6a shows the x-direction displacement field of particles at times of 0.1 s, 0.3 s and 1 s of fracture propagation in the base case simulation. Fracture initiates from the fluid injection point and opens at several locations preferentially perpendicular to the minimum principal stress σ_{min}. Similar to experiments [29,72], our simulation shows complex and sub-parallel fractures induced by the fluid drag force. Fig. 6b shows that the fluid flow is localized in the opened fracture channels and fluid drag supports the aperture of fracture walls. Stopping fluid injection would result in loss of drag forces, relaxation of the particles, and therefore closure of the fracture.

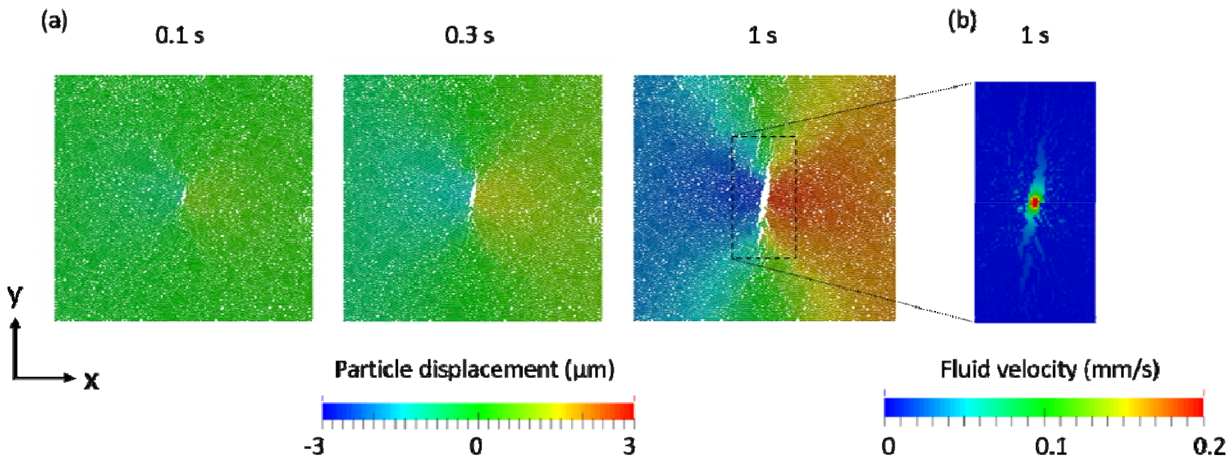

Figure 6. (a) Fracture initiation and propagation represented by the particle x-direction displacement field at times of 0.1 s, 0.3 s and 1 s in the base case. (b) Field of fluid velocity magnitude. The injection velocity is 1 mm/s. The upper limit shown in the figure is selected as 0.2 mm/s to better visualize the velocity field far from the inlet port.

Unlike cemented materials, the uncemented particle packing has no tensile strength. Experiments have shown that the fracture initiation in a packing of uncemented particles is determined by fluid invasion and shear failure ahead of the fracture tip [29,73,74]. Therefore, shear strain localization in the particle packing is critical to explain fracturing in uncemented granular packings. We use open source digital image correlation tools (2D-DIC MATLAB codes Ncorr) [75] and calculate the shear and volumetric strains from the images produced by DEM numerical simulations. Fig. 7 shows the fields of local shear strain ε_{xy} and volumetric strain ε_{vol} of the full domain at the time of 0.3 s taking time 0 s as the reference frame. A sheared zone near the fracture face indicates that the fracture opening in unconsolidated particles is dominated by shear failure.

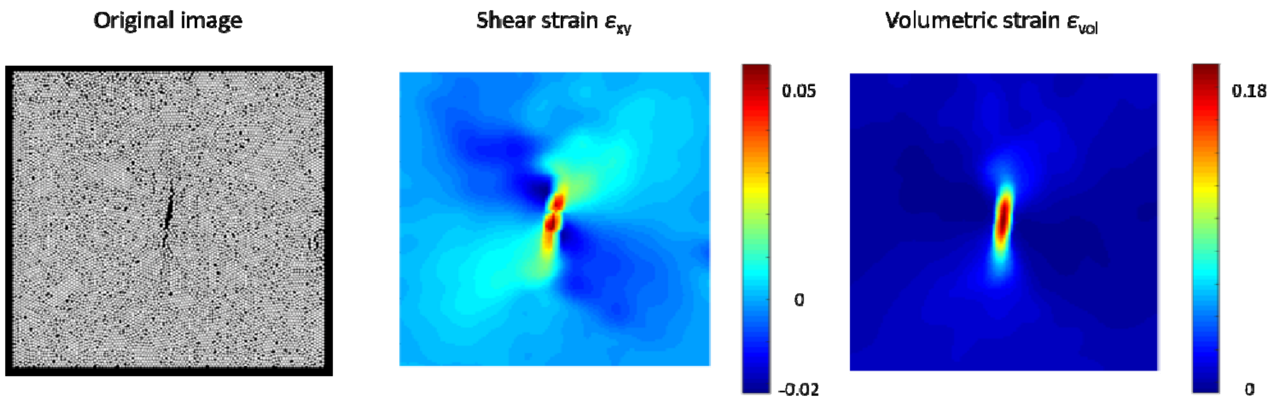

Figure 7. Fields of shear strain ε_{xy} and volumetric strain ε_{vol} obtained from DEM simulation results based on the 2D-DIC.

4.2 Control factors on fluid-driven fractures in granular media

Fluid-driven fracture opening in granular media exhibits large deformations and irrecoverable deformations. The classical theory of linear elastic fracture mechanics coupled with poroelasticity is not applicable for this problem. The resolved CFD-DEM model offers an alternative to investigate fracture initiation and explore grain-scale processes. As illustrated in Section 1, the dimensionless variable F_s/F_{sk} (ratio of seepage force and skeletal force) is a criterion to separate regimes of fluid invasion without fracturing and drag-driven fracture opening. In this section, we will explore effects of the dimensionless variable F_s/F_{sk} along with other important parameters.

First, the simulations explore the dimensionless variable F_s/F_{sk} from 0.75 to 75 by increasing the fluid viscosity from 0.1 Pa·s to 10 Pa·s. All other parameters stay invariant (Table 2). Fig. 8 shows the displacement patterns for tests at the same time t = 0.3 s but with a different F_s/F_{sk}. When the F_s/F_{sk} is relatively small ~ 0.75, the particles exhibit negligible displacements which result in near zero shear and volumetric strains. The injected fluid from the middle point tends to invade rather than displace the particle packing. For this case scenario, the flow regime is dominated by the infiltration rather than the fracture opening.

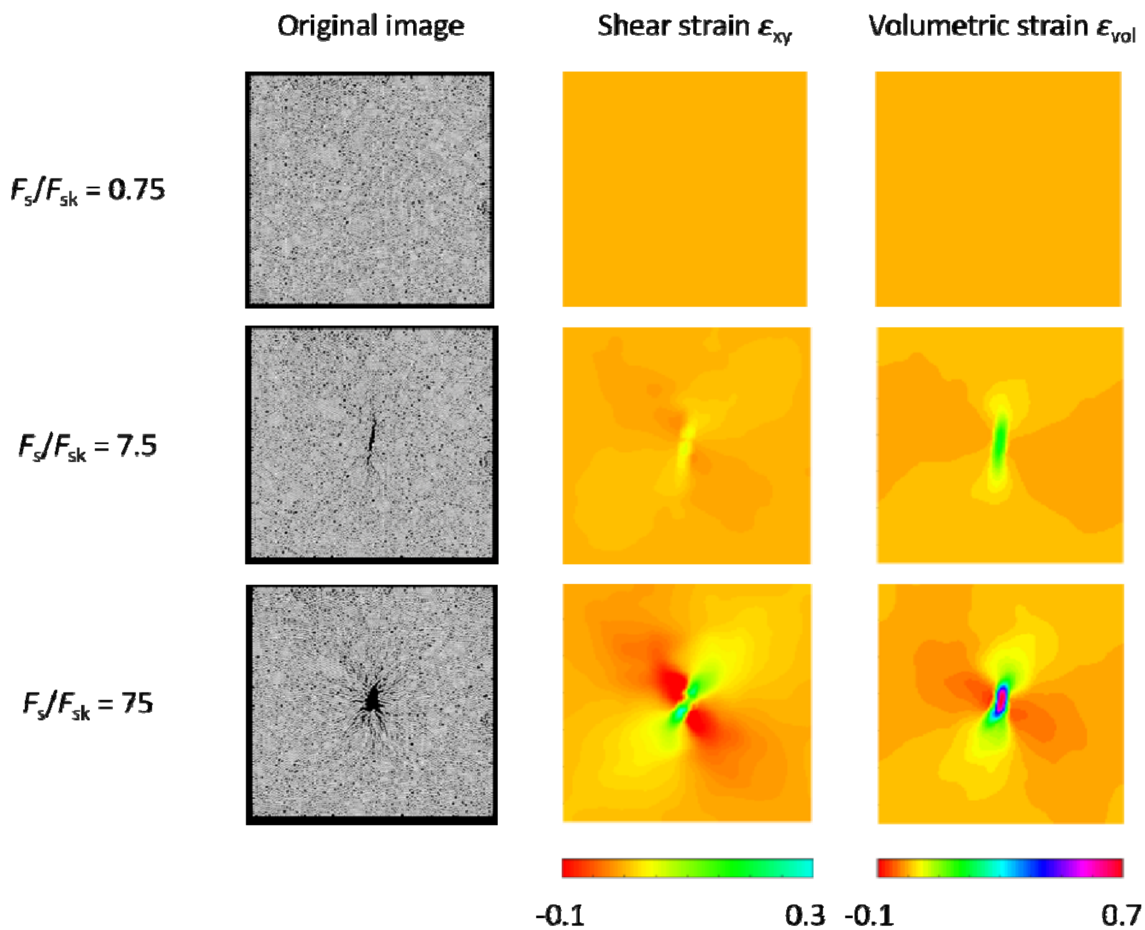

Figure 8. Effect of the dimensionless variable F_s/F_{sk} on the fracture opening. From top to bottom, F_s/F_{sk} changes from 0.75, 7.5 and 75. The simulated time of all three cases is 0.3 s.

As the F_s/F_{sk} increases from 0.75 to 7.5, a fracture opening occurs, which indicates a transition from the infiltration-dominated regime to the grain-displacement dominated regime. The created fracture is relatively complex with a main opening and several branches. The fracture initiates at the fluid injection point and opens up perpendicularly to the minimum principal stress direction. The field of local shear strain shows that the fluid also permeates into the granular medium and induces a shearing of the particles near the main fracture. The highly sheared zone coincides with the created fractures. As the F_s/F_{sk} further increases to 75, the fluid flow induces a short and wide cavity rather than thin fractures as seen for F_s/F_{sk} = 7.5. High fluid viscosity inhibits infiltration, therefore, fluid injection results in a grain-displacement dominated regime. The particle displacements induced by seepage drag forces lead to changes in effective stress.

Apart from the dimensionless parameter F_s/F_{sk}, the particle micromechanical properties including Young's modulus, Poisson's ratio and friction coefficient may also influence the fracture opening behavior. The base case shown in Fig. 9a uses the parameters given in Table 2. Fig. 9b shows the simulation result by increasing the particle Young's modulus from 1 MPa to 10 MPa. The created openings tend to be thin for a granular medium consisting of stiff particles, which also manifests by the small sheared zone and the low-magnitude volumetric strains. Therefore, an increase in particle Young's modulus reduces the width of fracture opening.

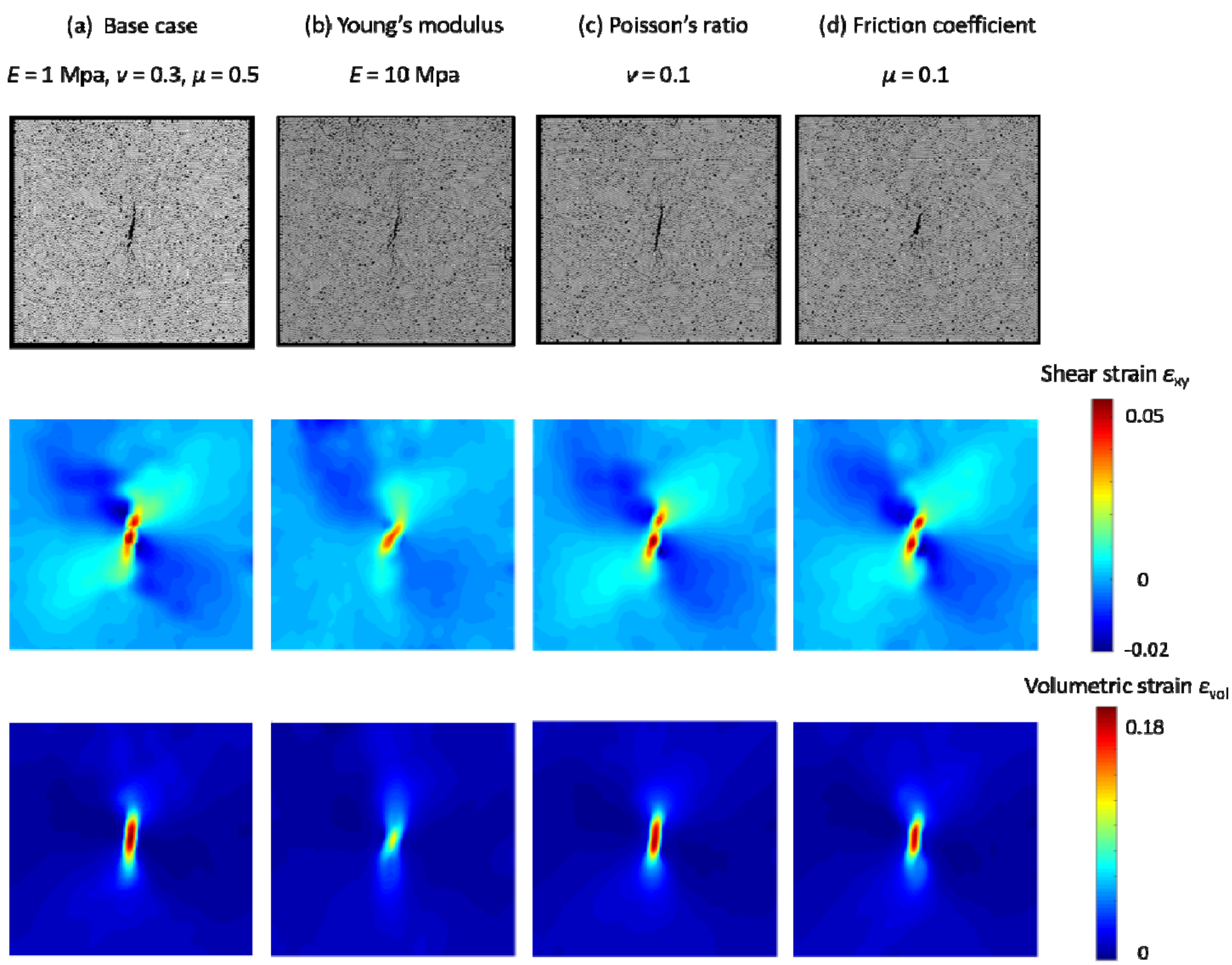

Figure 9. Effects of particle micromechanical properties on the fields of shear and volumetric strains. Compared to base case (a) with parameters given in Table 2, case (b)-(d) indicate that Young's modulus among other micromechanical parameters has the most significant influence on fluid-driven fracture behavior.

Fig. 9c shows the simulation result by decreasing the particle Poisson's ratio from 0.3 to 0.1. The particle Poisson's ratio only has a slight impact on the fracture opening. Fig. 9d shows the simulation result by decreasing the coefficient of friction from 0.5 to 0.1. The coefficient of friction μ is proportional to the roughness of particle surface. As μ decreases, the shear and volumetric strains show a slight decrease due to the decrease in particle surface roughness. This is consistent with fact that the friction angle is proportional to the dilation angle in granular media [76,77]. Fig. 9 shows that the Young's modulus among other micromechanical properties shows the most significant influence on fluid-driven fracture behavior.

4.3 Regimes of fracture opening

Injection of aqueous glycerin solutions into dense dry Ottawa F110 sand showed that the flow regime depends on the interplay between fluid infiltration and grain displacement [70]. The flow regime is dominated by the infiltration with negligible flow channels when the injection velocity and the fluid viscosity are relatively small. A transition from the infiltration-dominated regime to the grain-displacement dominated regime occurs as the injection velocity and the fluid viscosity increase, which is consistent with our simulation results. The classification of these displacement regimes in unconsolidated granular media shares similarities with that of fracture propagation regimes in cemented rocks [25,78].

The dimensionless time τ_1, defined as the ratio between the diffusion time from hydromechanical coupling t_d and the injection time t_i, serves to classify the infiltration-dominated and the grain-displacement dominated regimes [70].

$$\tau_1 = \frac{t_d}{t_i} = \frac{\mu_f u l}{Ek} \tag{6}$$

$$t_d = \frac{\mu_f l^2}{Ek} \tag{7}$$

$$t_i = \frac{l}{u} \tag{8}$$

where μ_f is the fluid viscosity, u is the injection velocity, l is the characteristic length, E is the small strain Young's modulus of the granular packing and k is the permeability. The fluid injection inlet diameter is the characteristic length [70]. The Young's modulus of the medium is proportional to the particle Young's modulus when the particle Poisson's ratio is constant [35]. We measure the effective medium modulus of the particle monolayer by performing biaxial compression test based on the Kozeny-Carman relation (see details in the supplementary material). The permeability of the particle packing is a function of particle size and packing porosity. We include the specific values of Young's modulus and permeability of the granular medium for each case scenario in the supplementary material.

We investigate effects of all relevant parameters such as the fluid viscosity, injection velocity, particle micromechanical properties, particle size and applied stress in our simulations of fracture propagation. Only the fluid viscosity and the injection velocity were varied in the experiments performed by Huang et al. (2012a). For each case scenario, we calculate the dimensionless parameters τ_1 and F_s/F_{sk} and summarize all results in Fig. 10. The supplementary material includes a table listing the properties used for each numerical simulation.

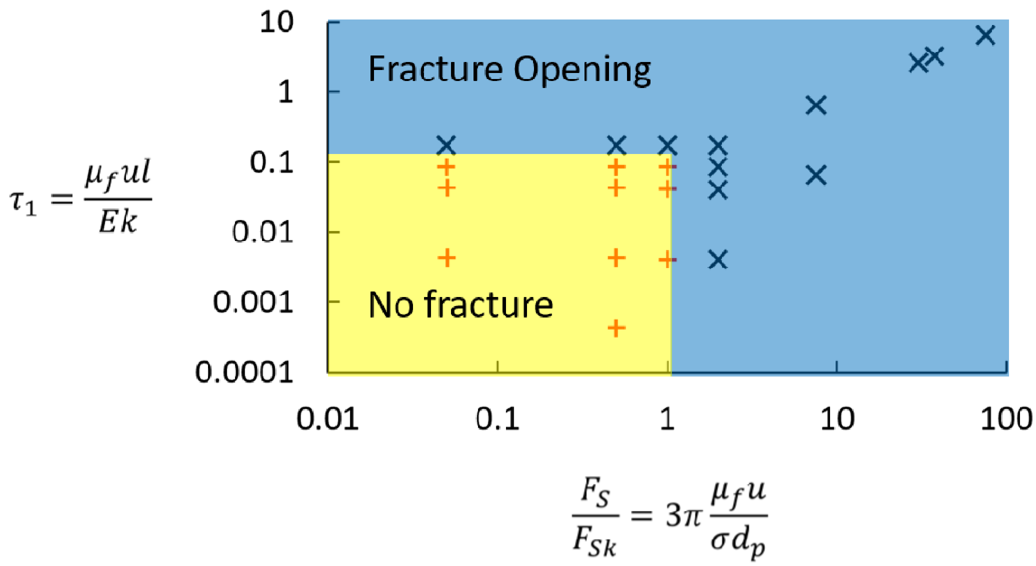

Figure 10. Regimes of fracture/cavity opening in granular media based on the dimensionless parameters τ_1 and F_s/F_{sk}. Each point results from one simulation using various parameters including the fluid viscosity μ_f, injection velocity u, Young's modulus E, particle size d_p/permeability k and applied stress σ. There are two clear zones of fracture opening and no fracture opening.

Fig. 10 shows that the dimensionless parameter τ_1 or F_s/F_{sk} alone is not sufficient to describe the displacement regimes of fluid injection into a packing of particles. For instance, a fracture opening initiates in a relatively soft granular medium when F_s/F_{sk} is smaller than 1 as long as τ_1 is large enough. The results show that these two dimensionless parameters in combination result in a good indicator of fracture opening. We find a simple and straightforward criterion conditioning the fracture opening: $\tau_1 > 0.17$ or $F_s/F_{sk} > 1$. The threshold value of τ_1 is numerically and experimentally obtained as 0.44 and 0.1, in the literature [35,72], which is consistent with our results. The valid range of the injection rate could be broad as long as the flow is in a laminar regime (small Reynold's number). For instance, an injection rate of 125 ml/min and 9.6×10^6 ml/min has been used to characterize the dimensionless time τ_1 in the literature [35,70,72]. The threshold value of F_s/F_{sk} indicates that the seepage force should be greater than the skeletal force [58]. Fig. 10 provides a simple approach to predict whether a fracture opening will occur in granular media and has a wide range of applications. For instance, honey (~10,000 cp at room temperature) injected at 0.1 m/s may fracture sands of 1 mm size under a confining stress of 5 KPa because the calculated F_s/F_{sk} exceeds 1.

5. Concluding Remarks

We investigate numerically the fracture initiation mechanisms in a granular medium subjected to constant boundary stresses and to fluid injection with a localized source. The dimensionless parameter F_s/F_{sk}, which takes into account the impact of fluid viscosity, injection velocity, grain size and principal effective stresses, serves as an indicator of drag-driven fracture opening [58]. On the other hand, simulation results show that grain micromechanical properties such as Young's modulus of granular packing can also influence the fracture initiation and propagation. The dimensionless time τ_1 characterizes a similar impact of Young's modulus as observed in the numerical simulations [70]. Therefore, we combine these two dimensionless parameters F_s/F_{sk} and τ_1 to classify the regimes of fracture opening in uncemented granular media. We find a simple and straightforward criterion: a drag-driven fracture opening occurs when $\tau_1 > 0.17$ or $F_s/F_{sk} > 1$. The dimensionless thresholds are valid for various types of granular media and injection conditions.

Acknowledgement

This material is based upon work supported as part of the Center for Frontiers of Subsurface Energy Security, an Energy Frontier Research Center funded by the U.S. Department of Energy, Office of Science, and Office of Basic Energy Sciences under Award Number DE-SC0001114. The authors would also like to thank Texas Advanced Computing Center (https://www.tacc.utexas.edu/) for providing high performance computing facilities.

References

[1] S. Bachu, Prog. Energy Combust. Sci. **34**, 254 (2008).

[2] S. D. Hovorka, S. M. Benson, C. Doughty, B. M. Freifeild, S. Sakurai, T. M. Daley, Y. K. Kharaka, M. H. Holtz, R. C. Trautz, H. S. Nance, L. R. Myer, and K. G. Knauss, Environ. Geosci. **13**, 105 (2006).

[3] S. K. A. Au, K. Soga, M. R. Jafari, M. D. Bolton, and K. Komiya, J. Geotech. Geoenvironmental Eng. **129**, 254 (2003).

[4] N. L. Germanovich and C. L. Murdoch, Proc. R. Soc. A Math. Phys. Eng. Sci. **466**, 3225 (2010).

[5] L. W. Lake, *Enhanced Oil Recovery* (1989).

[6] R. G. Keck, SPE Annu. Tech. Conf. Exhib. 12 (2002).

[7] C.-F. Tsang, J. Birkholzer, and J. Rutqvist, Environ. Geol. **54**, 1723 (2008).

[8] M. J. Economides and K. G. Nolte, *Reservoir Stimulation* (Prentice Hall Englewood Cliffs, New Jersey, 1989).

[9] J. A. Ayoub, J. M. Kirksey, B. P. Malone, and W. D. Norman, SPE Form. Damage Control Symp. (1992).

[10] S. Tong and K. K. Mohanty, Fuel **181**, 463 (2016).

[11] Y. He, S. Cheng, L. Li, G. Mu, T. Zhang, H. Xu, J. Qin, and H. Yu, SPE Reserv. Eval. Eng. **20**, 708 (2017).

[12] H. Tang, J. E. Killough, Z. Heidari, and Z. Sun, SPE J. **22**, 1034 (2017).

[13] A. J. Kopf, Rev. Geophys. **40**, 2 (2002).

[14] L. I. Dimitrov, Earth-Science Rev. **59**, 49 (2002).

[15] A. Hurst, J. Cartwright, and D. Duranti, Geol. Soc. London, Spec. Publ. **216**, 123 LP (2003).

[16] R. J. H. Jolly and L. Lonergan, J. Geol. Soc. London. **159**, 605 LP (2002).

[17] A. K. Jain and R. Juanes, J. Geophys. Res. Solid Earth **114**, (2009).

[18] I. R. MacDonald, N. L. Guinasso Jr., R. Sassen, J. M. Brooks, L. Lee, and K. T. Scott, Geology **22**, 699 (1994).

[19] A. M. Tréhu, C. Ruppel, M. Holland, G. R. Dickens, M. E. Torres, T. S. Collett, D. Goldberg, M. Riede, and P. Schultheiss, Oceanography **19**, (2006).

[20] M. J. Osborne and R. E. Swarbrick, Am. Assoc. Pet. Geol. Bull. **81**, 1023 (1997).

[21] D. D. Pollard, Tectonophysics **19**, 233 (1973).

[22] A. M. Rubin, Annu. Rev. Earth Planet. Sci. **23**, 287 (1995).

[23] C. H. Yew and X. Weng, *Mechanics of Hydraulic Fracturing* (Gulf Professional Publishing, 2014).

[24] J. Adachi, E. Siebrits, A. Peirce, and J. Desroches, Int. J. Rock Mech. Min. Sci. **44**, 739 (2007).

[25] E. Detournay, Int. J. Geomech. **4**, 35 (2004).

[26] M. B. Smith, M. Bose, H. H. Klein, B. R. Ozenne, and R. S. Vandersypen, SPE Int. Symp. Exhib. Form. Damage Control 11 (2004).

[27] E. Hoek and C. D. Martin, J. Rock Mech. Geotech. Eng. **6**, 287 (2014).

[28] J. Desroches, E. Detournay, B. Lenoach, P. Papanastasiou, J. R. A. Pearson, M. Thiercelin, and A. Cheng, Proc. R. Soc. London. Ser. A Math. Phys. Sci. **447**, 39 (1994).

[29] M. Khodaverdian and P. McElfresh, SPE Annu. Tech. Conf. Exhib. 13 (2000).

[30] M. S. Bruno, A. Dorfmann, K. Lao, and C. Honeger, in *DC Rocks 2001, 38th US Symp. Rock Mech.* (American Rock Mechanics Association, 2001).

[31] L. Jing and J. A. Hudson, Int. J. Rock Mech. Min. Sci. **39**, 409 (2002).

[32] P. A. Cundall and O. D. L. Strack, Géotechnique **29**, 47 (1979).

[33] D. O. Potyondy and P. A. Cundall, Int. J. Rock Mech. Min. Sci. **41**, 1329 (2004).

[34] I. Fatt, Pet. Trans. **207**, 144 (1956).

[35] F. Zhang, B. Damjanac, and H. Huang, J. Geophys. Res. Solid Earth **118**, 2703 (2013).

[36] E. Catalano, B. Chareyre, and E. Barthélemy, Int. J. Numer. Anal. Methods Geomech. **38**, 51 (2014).

[37] H. Shimizu, S. Murata, and T. Ishida, Int. J. Rock Mech. Min. Sci. **48**, 712 (2011).

[38] E. Papachristos, L. Scholtès, F. V Donzé, and B. Chareyre, Int. J. Rock Mech. Min. Sci. **93**, 163 (2017).

[39] J. S. Yoon, A. Zang, and O. Stephansson, Geothermics **52**, 165 (2014).

[40] M. Mansouri, J.-Y. Delenne, M. S. El Youssoufi, and A. Séridi, Comptes Rendus Mécanique **337**, 675 (2009).

[41] D. F. Boutt, B. K. Cook, and J. R. Williams, Int. J. Numer. Anal. Methods Geomech. **35**, 997 (2011).

[42] X. Sun, M. Sakai, and Y. Yamada, J. Comput. Phys. **248**, 147 (2013).

[43] M. Robinson, M. Ramaioli, and S. Luding, Int. J. Multiph. Flow **59**, 121 (2014).

[44] D. Markauskas, H. Kruggel-Emden, R. Sivanesapillai, and H. Steeb, Powder Technol. **305**, 78 (2017).

[45] J. W. Fernandez, P. W. Cleary, M. D. Sinnott, and R. D. Morrison, Miner. Eng. **24**, 741 (2011).

[46] T. Bluhm-Drenhaus, E. Simsek, S. Wirtz, and V. Scherer, Chem. Eng. Sci. **65**, 2821 (2010).

[47] Y. Han and P. A. Cundall, Int. J. Numer. Anal. Methods Geomech. **37**, 1391 (2013).

[48] F. Wissing, S. Wirtz, and V. Scherer, Fuel **206**, 638 (2017).

[49] T. Shan and J. Zhao, Acta Mech. **225**, 2449 (2014).

[50] M. Ebrahimi and M. Crapper, Particuology **31**, 15 (2017).

[51] F. Zhou, S. Hu, Y. Liu, C. Liu, and T. Xia, Particuology **16**, 196 (2014).

[52] A. Hager, C. Kloss, S. Pirker, and C. Goniva, J. Comput. Multiph. Flows **6**, 13 (2014).

[53] S. Mondal, C.-H. Wu, and M. M. Sharma, Int. J. Multiph. Flow **84**, 245 (2016).

[54] Z. Y. Zhou, S. B. Kuang, K. W. Chu, and A. B. Yu, J. Fluid Mech. **661**, 482 (2010).

[55] D. A. Lockner, J. D. Byerlee, V. Kuksenko, A. Ponomarev, and A. Sidorin, Nature **350**, 39 (1991).

[56] P. M. Benson, S. Vinciguerra, P. G. Meredith, and R. P. Young, Science (80-.). **322**, 249 (2008).

[57] H. Daigle, N. W. Hayman, E. D. Kelly, K. L. Milliken, and H. Jiang, Geophys. Res. Lett. **44**, 2167 (2017).

[58] H. Shin and J. C. Santamarina, Earth Planet. Sci. Lett. **299**, 180 (2010).

[59] C. Kloss, C. Goniva, A. Hager, S. Amberger, and S. Pirker, Prog. Comput. Fluid Dyn. an Int. J. **12**, 140 (2012).

[60] H. P. Zhu, Z. Y. Zhou, R. Y. Yang, and A. B. Yu, Chem. Eng. Sci. **62**, 3378 (2007).

[61] Z. Sun, D. N. Espinoza, and M. T. Balhoff, J. Geophys. Res. Solid Earth **121**, 7867 (2016).

[62] Z. Sun, D. N. Espinoza, M. T. Balhoff, and T. A. Dewers, Rock Mech. Rock Eng. **50**, 3337 (2017).

[63] Y. Keehm, *Computational Rock Physics: Transport Properties in Porous Media and Applications* (2003).

[64] P. Meakin and A. M. Tartakovsky, Rev. Geophys. **47**, (2009).
[65] A. A. Shirgaonkar, M. A. MacIver, and N. A. Patankar, J. Comput. Phys. **228**, 2366 (2009).
[66] C. W. MacMinn, E. R. Dufresne, and J. S. Wettlaufer, Phys. Rev. X **5**, 11020 (2015).
[67] O. Coussy, *Poromechanics* (John Wiley & Sons, 2004).
[68] Z. Sun, *Investigation of Coupled Chemo-Hydro-Mechanical Processes with Discrete Element Modeling* (2019).
[69] J. E. Olson, J. Holder, and M. Hosseini, SPE Hydraul. Fract. Technol. Conf. 9 (2011).
[70] H. Huang, F. Zhang, P. Callahan, and J. Ayoub, Phys. Rev. Lett. **108**, 258001 (2012).
[71] Á. Kézdi and L. Réth才áti, *Handbook of Soil Mechanics* (Elsevier Amsterdam, 1974).
[72] H. Huang, F. Zhang, P. Callahan, and J. A. Ayoub, SPE J. **17**, 903 (2012).
[73] Z. Zhai and M. M. Sharma, SPE Annu. Tech. Conf. Exhib. 14 (2005).
[74] R. S. Hurt and L. N. Germanovich, SPE Annu. Tech. Conf. Exhib. (2012).
[75] J. Blaber, B. Adair, and A. Antoniou, Exp. Mech. **55**, 1105 (2015).
[76] K. H. Andersen and K. Schjetne, J. Geotech. Geoenvironmental Eng. **139**, 1140 (2012).
[77] T. Schanz and P. A. Vermeer, Géotechnique **46**, 145 (1996).
[78] J. I. Adachi and E. Detournay, Eng. Fract. Mech. **75**, 4666 (2008).